PHYSICAL REVIEW B **84**, 094106 (2011)

Distribution of unresolvable anisotropic microstructures revealed in visibility-contrast images using x-ray Talbot interferometry

Wataru Yashiro,[*] Sébastien Harasse, Katsuyuki Kawabata, Hiroaki Kuwabara, Takashi Yamazaki, and Atsushi Momose
Department of Advanced Materials Science, Graduate School of Frontier Sciences, the University of Tokyo, 5-1-5 Kashiwanoha, Kashiwa, Chiba 277-8561, Japan

(Received 5 April 2011; revised manuscript received 11 August 2011; published 19 September 2011)

X-ray Talbot interferometry has been widely used as a technique for x-ray phase imaging and tomography. We propose a method using this interferometry for mapping distribution of parameters characterizing anisotropic microstructures, which are typically of the order of μm in size and cannot be resolved by the imaging system, in a sample. The method uses reduction in fringe visibility, which is caused by such unresolvable microstructures, in moiré images obtained using an interferometer. We applied the method to a chloroprene rubber sponge sample, which exhibited uniaxial anisotropy of reduced visibility. We measured the dependencies of reduced visibility on both the Talbot order and the orientation of the sample and obtained maps of three parameters and their anisotropies that characterize the unresolvable anisotropic microstructures in the sample. The maps indicated that the anisotropy of the sample's visibility contrast mainly originated from the anisotropy of the microstructure elements' average size. Our method directly provides structural information on unresolvable microstructures in real space, which is only accessible through the ultra-small-angle x-ray scattering measurements in reciprocal space, and is expected to be broadly applied to material, biological, and medical sciences.

DOI: 10.1103/PhysRevB.84.094106 PACS number(s): 61.05.cf, 87.59.−e, 07.60.Ly

I. INTRODUCTION

For more than one hundred years, x-rays have been used for nondestructively visualizing internal structures in a wide range of fields including physics, chemistry, biology, and medicine. Conventionally, absorption of x-rays has been used for imaging applications, but in the early 1990s several imaging techniques using x-ray phase shift were proposed. These so-called x-ray phase imaging techniques have been highlighted because they are sensitive to light elements three orders of magnitude higher than that of absorption-contrast imaging (for example, Refs. 1–3). However, most of these techniques essentially require a highly brilliant synchrotron x-ray source. Recently, x-ray phase imaging using transmission grating (e.g., x-ray Talbot and Talbot-Lau interferometry) has been attracting attention because it can work with polychromatic and cone beams and has wide applications.[4–35] In x-ray Talbot (-Lau) interferometry, we can retrieve two quantitative images by using a fringe-scanning (phase-stepping) technique,[36–38] i.e., absorption and differential-phase images, from a series of experimentally obtained moiré images. Pfeiffer *et al.* have proposed another approach for generating image contrast, in which they quantified the relative decrease in fringe visibility in a moiré image by defining normalized visibility.[12] They reported that visibility contrast is generated through small-angle x-ray scattering from a microstructure with a scale much smaller than the spatial resolution of the imaging system. Their approach is fascinating because it can provide structural information inaccessible from absorption and differential phase images, and it is promising for a broad range of applications.[39–50] However, no general formulation of this phenomenon, which is essential for quantitative structure analysis, had been provided.

In one of our previous papers,[51] we showed that the reduction in fringe visibility can be formulated using an autocorrelation function that describes the spatial fluctuations of the wavefront caused by the unresolvable microstructures. Experimentally obtained reduced visibilities for several samples with isotropic microstructures successfully fit with our formula. The spatial fluctuations were characterized using three parameters: correlation length, the Hurst exponent, and variance. The correlation length can be interpreted as the average size of the microstructure elements, the Hurst exponent is related to their average shape, and the variance is proportional to their scattering power in the forward direction. Our results showed that the reduced visibility can be used for quantitatively analyzing unresolvable microstructures in the order of μm size.

We applied this concept to a cylindrical chloroprene rubber (CR) sponge sample in the current research. It exhibited uniaxial anisotropy of visibility contrast, that is, we observed change in the sample's visibility contrast when rotating it around the optical axis of the interferometer with its cylinder axis not parallel to the optical axis. We obtained maps for the parameters characterizing the unresolvable anisotropic microstructures in the sample that caused visibility contrast. Similar to our previous paper,[51] optimal values for the three parameters that characterize the phase fluctuations due to the unresolved microstructures were obtained for each pixel of a projection image at an orientation of the sample. By rotating the cylinder axis of the sample around the optical axis, we also obtained the dependencies of the three parameters on the sample orientation. Sine functions were fitted to these orientation dependencies, and maps that represent distributions of the three parameters and their anisotropies were finally obtained. We found that the correlation length and the Hurst exponent exhibited anisotropies and the former was more anisotropic than the latter, but the variance did not. These results indicated that the anisotropy of the sample's visibility contrast mainly originated from the anisotropy of the microstructure elements' average size.

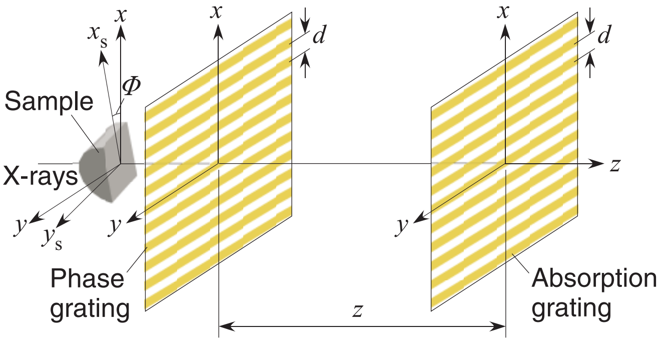

FIG. 1. (Color online) Schematic illustration of experimental setup of x-ray Talbot interferometry

II. THEORETICAL BACKGROUND

First, we briefly review the general formula for the reduced visibility provided in our previous paper.[51] For simplicity, we considered the x-ray Talbot interferometer system for plane-wave illumination (wavelength: λ) as schematically illustrated in Fig. 1. We define d and z by the pitch of the gratings and the distance between them. The distance z can be expressed by pd^2/λ for the plane-wave illumination, where p is called the Talbot order. We assumed that a sample is placed just in front of the first grating and a detector is located just behind the second grating. For convenience, we define xy-coordinate systems on planes perpendicular to the optical axis (the z axis), the x axis of which is in the direction perpendicular to the lines of the first grating.

Our basic idea was to formulate reduced visibility by unresolvable spatial fluctuations of the wavefront due to microstructures in a sample. To discuss the effect of the wavefront's spatial fluctuations (phase fluctuations), we express the phase shift $\phi(x,y)$ caused by the sample (i.e., the wavefront just behind the sample) as the sum of smooth (resolvable) and fine (unresolvable) features, $\phi_s(x,y) + \phi_f(x,y)$.[52] Normalized visibility, which is defined by the ratio of visibility with the sample (V) to that without the sample (V_0), is then approximately given by

$$\frac{V}{V_0} \approx \overline{e^{i\Delta\phi_f(x,y;pd)}}, \tag{1}$$

where $\Delta\phi_f(x,y;pd) \equiv \phi_f(x,y) - \phi_f(x+pd,y)$and the bar means averaging around (x,y) within the spatial resolution of the detector. If we assume that ϕ_f can be modeled as a random Gaussian variable,[52,53] the width of which is given by σ, then

$$\frac{V}{V_0} \approx e^{-\sigma^2(x,y)\{1-\gamma(x,y;pd)\}}, \tag{2}$$

where $\gamma(x,y;X)$ is the normalized autocorrelation function at two points separated by X in the x direction, which is given by

$$\gamma(x,y;X) \equiv \frac{\overline{\phi_f(x,y)\phi_f(x+X,y)}}{\sigma^2}. \tag{3}$$

Thus, the reduced visibility can be generally formulated in terms of the autocorrelation function of the wavefront's spatial fluctuations. These results are also valid for spherical-wave illumination[54] if (x,y) is regarded as the coordinate just behind the sample and pd in Eqs. (1) and (2) is replaced by

$$\begin{cases} pd_1\frac{R_{s0}}{R_{10}} & \text{(for a sample placed in front of the first grating)} \\ pd_1\frac{R_{s2}}{R_{12}} & \text{(for a sample placed behind the first grating),} \end{cases} \tag{4}$$

where d_1 is the pitch of the first grating, R_{s0} (R_{s2}) is the distance of the sample from the x-ray source (from the second grating), and R_{10} (R_{12}) is the distance of the first grating from the x-ray source (from the second grating). Note that from Eq. (2), V/V_0 approaches zero when σ increases. In addition, for a given sample, V/V_0 is a function of pd. Furthermore, it is trivial that $\gamma(X) \approx \gamma(-X)$, that is, γ has inversion symmetry. This means that when a sample is rotated around the optical axis and V/V_0 is experimentally obtained as a function of the rotation angle Φ, V/V_0 has a period of π; therefore, it can be generally expressed by a Fourier series.

It should also be noted that, as shown in our previous paper,[51] the Fourier transform of V/V_0 with respect to pd corresponds to the angular distribution of ultra-small-angle x-ray scattering (USAXS) integrated in the direction parallel to the grating lines. That is, Eq. (1) is related to the angular distribution of USAXS by

$$\int I_{\mathrm{USAXS}}(x,y;k_x,k_y)dk_y \propto \int \overline{e^{i\Delta\phi_f(x,y;X)}}\exp\left[ik_xX\right]dX, \tag{5}$$

where k_x and k_y are the momentum transfers parallel and perpendicular to the x direction, and $I_{\mathrm{USAXS}}(x,y;k_x,k_y)$ is the intensity of the ultra-small-angle scattering for (k_x,k_y) from a small volume at (x,y), the size of which is comparable to the spatial resolution of the detector. The parameter X corresponds to pd in Eq. (1). Next, we introduce a rotation Φ of the sample around the optical axis. In this case, it is convenient to define a coordinate system (x_s,y_s) attached to the sample in the plane perpendicular to the optical axis, as shown in Fig. 1. Because Eq. (1) depends on the rotation angle Φ, we explicitly write the right hand side of Eq. (1) by $\overline{e^{i\Delta\phi_f(x_s,y_s;X,\Phi)}}$. We can now consider that the direction of X (or the direction perpendicular to the grating lines) is rotated with respect to the x_sy_s coordinate. The intensity of USAXS is then given by

$$I_{\mathrm{USAXS}}(x_s,y_s;k_x,k_y) \propto \iint \overline{e^{i\Delta\phi_f(x_s,y_s;X,\Phi)}}\exp[ik_xX]|X|dXd\Phi. \tag{6}$$

We used the projection-slice theorem. Thus, we can obtain structural information on unresolvable microstructures that is equivalent to that obtained from the measurement of USAXS.

Because the normalized autocorrelation function γ is obtained from projections of unresolvable microstructures [$\phi_f(x,y)$ in Eq. (3)] in the projection approximation, we can obtain structural information on the microstructures by measuring reduced visibility. In fact, γ takes a maximum value ($=1$) when $X = 0$ and approaches 0 when $X \to \infty$; therefore,

γ has a finite width around $X = 0$. This width corresponds to the correlation length of the wavefront's spatial fluctuations in the x direction, within which the projection $\phi_f(x,y)$ is correlated with itself. If a microstructure can be regarded as an ensemble of unresolvable microstructure elements, the size of which are comparable to pd, the correlation length can then be related to the average size of the projections of the unresolved microstructure elements in the x direction. In fact, if the microstructure elements are approximately represented by particles, the positions and directions of which are independent of each other, the correlation length characterizes the average size of the particle projections in the x direction. A simple model suitable for describing the behavior of γ was proposed by Sinha *et al.*[55]:

$$\gamma(x,y;X) \approx \exp[-\{|X|/\xi(x,y)\}^{2H}], \tag{7}$$

where ξ corresponds to the correlation length of the phase fluctuations, defining the width of γ, and H is called the Hurst exponent ($0 < H < 1$), defining the shape of γ near $X = 0$. In our previous paper,[51] ξ and H were quantitatively related to the average sizes and shapes of the unresolvable microstructure elements for several samples. Note that σ^2 in Eq. (2) is proportional to the scattering power of the microstructures in the forward direction.

If microstructures in a sample have anisotropy, then σ^2 and γ in Eq. (2) can change with a rotation of the sample around the optical axis. In this case, we can explicitly express them by $\sigma^2(x_s,y_s;\Phi)$ and $\gamma(x_s,y_s;X,\Phi)$:

$$\frac{V}{V_0} \approx \exp[-\sigma^2(x_s,y_s;\Phi)\{1-\gamma(x_s,y_s;X,\Phi)\}]|_{X=pd}. \tag{8}$$

Although the directions of the microstructure elements in the sample should not be perfectly random, Sinha's model should also be applied if the anisotropy is weak and the positions of the elements can be regarded as random.[56] In fact, for the sample discussed in the next section, the experimentally obtained pd dependencies of the normalized visibility for each pixel fitted well with Eq. (7). Thus, we can obtain maps of $\xi(x_s,y_s;\Phi)$, $H(x_s,y_s;\Phi)$, and $\sigma^2(x_s,y_s;\Phi)$ for an orientation Φ of the sample. By changing the orientation of the sample, we can also obtain maps of their anisotropies.

III. EXPERIMENT

In our previous papers,[51,57] we showed that experimental results for several unresolvable isotropic microstructures can be successfully explained using Sinha's model [Eq. (7)] in our formulation, and the three parameters required to characterize the spatial wavefront fluctuations were related to the physical properties of the microstructures. We applied this concept to a sample with unresolvable anisotropic microstructures.

The experiment was performed with synchrotron x-rays at beamline 14C at the Photon Factory, KEK, Japan (the experimental setup of x-ray Talbot interferometer is shown in Fig. 1). The incident x-rays were monochromatized with a double-crystal monochromator to 17 keV. A set of 5.3-μm-pitch gold gratings with a Ronchi ruling (a $\pi/2$-phase grating for the first grating and a 30-μm-thick absorption grating for the second grating) were used, and they were aligned parallel to each other. Moiré images generated by the two gratings were recorded using a charge coupled device (CCD)-based x-ray image detector (Spectral Instruments), where the CCD (4096 × 4096 pixels) was connected to a 40-μm-thick GOS ($Gd_2O_2S:$ Pr) screen with a 2:1 fiber coupling. The effective pixel size of the detector was 18 μm, and the width of the line spread function (LSF) of the detector was experimentally determined to be 70 μm. We used a five-step fringe scan[36] with an exposure time of 1 s each.

A cylindrical CR sponge with a diameter of 5 mm was used as the sample. The sample was cut into halves, and both halves were fixed on an acrylic plate and rotated around the optical axis. As shown in Fig. 2(a), one half was fixed with its cylinder axis parallel to the optical axis (upper figures), and the other with its cylinder axis perpendicular to the optical axis (lower figures). Figures 2(b), 2(c), and 2(d) are absorption, differential-phase, and visibility-contrast (normalized visibility) images for the two halves, respectively, obtained using the fringe-scanning technique.

Figure 3 shows dependencies of the visibility-contrast image on the orientations of the two halves [(a) $\Phi = 0°$, (b) $\Phi = 45°$, and (c) $\Phi = 90°$]. It can be seen that the visibilities of the upper images were almost constant, while those of the lower images changed due to the rotation of the sample. We also rotated the sample with its cylinder axis in other directions, and, as a result, this CR sponge had uniaxial anisotropy of the visibility contrast, the axis of which is parallel to the cylinder axis (we observed change in visibility when rotating the sample around the optical axis with its cylinder axis not parallel to the optical axis, and it changed the most when the cylinder axis was rotated in the plane perpendicular to the optical axis, like the lower images).

The anisotropy of the lower sample in Fig. 3 can be represented with a color map.[46,50] In Fig. 4(b), the experimentally obtained dependence of $-\ln(V/V_0)$ on Φ for a pixel in the square area in Fig. 4(a) is plotted. As mentioned in Sec. II, normalized visibility V/V_0 is a periodic function of the sample orientation Φ, the period of which is π; therefore, $-\ln(V/V_0)$ is expressed by a Fourier series. A sine function plus a constant (solid curve), that is, a Fourier series up to the first order, fitted the experimental data well. From such a least-squares fitting, we determined a sample orientation Φ_{min}, where $-\ln(V/V_0)$ takes the minimum value, and the amplitude of the sine function as well as the constant. Note that Φ_{min}, the amplitude, and the constant can also be obtained using the fringe-scanning technique, which was shown to be derived from the principle of least-squares estimation.[58] In Fig. 4(c), the anisotropy in the square area of the image in Fig. 4(a) [$-\ln(V/V_0)$ at $\Phi = 0°$] is displayed as a color map, where the color and brightness represent Φ_{min} and the amplitude of the sine function, respectively. The green tint of the entire area shows that the microstructures in the sample have anisotropy. Figure 4(d) is a map of the constant (corresponding to normalized visibility averaged over Φ). The brightness distribution of Fig. 4(d) seems to correlate with that of Fig. 4(c) but little with the color distribution of Fig. 4(c) (correlation coefficients were 0.58 for the former and 0.06 for the latter).

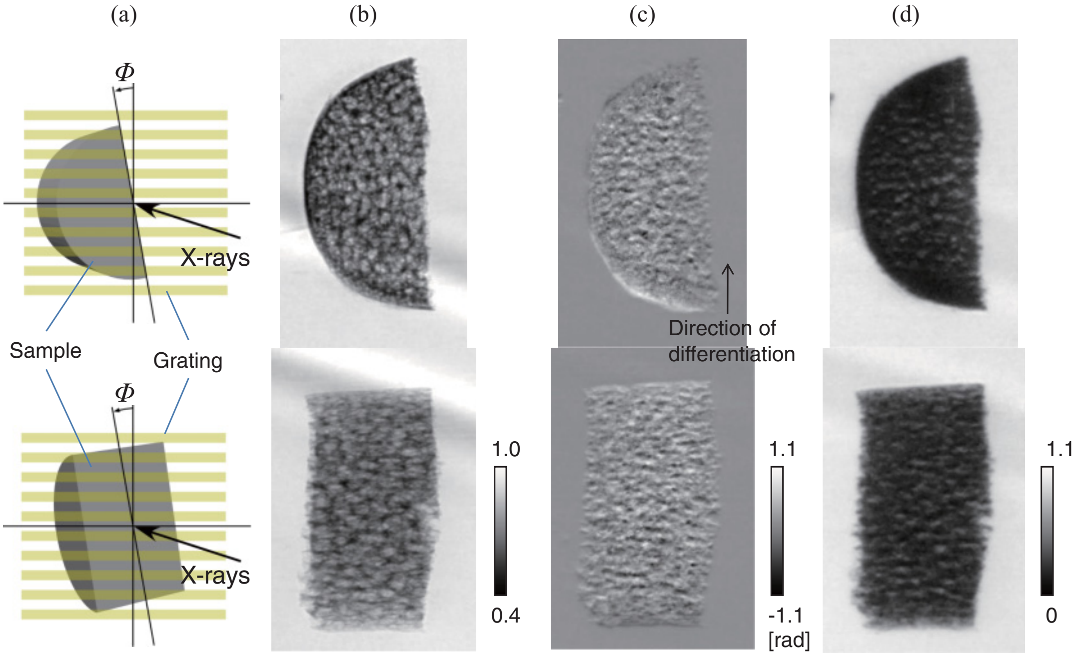

FIG. 2. (Color online) Schematic views of samples (a) and images obtained using x-ray Talbot interferometry at $\Phi = 0^\circ$ [(b) absorption, (c) differential-phase, and (d) visibility-contrast images]. In upper figures, cylinder axis of sample is parallel to optical axis, while in lower figures, it is perpendicular to optical axis. Talbot order p was fixed at 0.5.

It should be noted that the error bar $\Delta(V/V_0)$ of V/V_0 for each pixel was given by

$$\Delta\left(\frac{V}{V_0}\right) = \frac{V}{V_0}\sqrt{\frac{1}{M_s q_{0,0}}\left[\frac{1}{N_0}\left(1+\frac{1}{T}\right)+\frac{2}{V_0}\left(1+\frac{1}{T\,(V/V_0)}\right)\right]}, \tag{9}$$

where N_0 is the number of measurements without the sample, M_s is the number of steps of the fringe scan, $q_{0,0}$ is the average number of photons detected during the fringe scan without the sample, and T is the transmittance of the sample. This equation can be easily obtained for monochromatic x-rays from the analytical calculations in Ref. 15. To derive this equation, we assumed that the error is mainly due to photon statistics and that M_s is equal to or larger than 4. Practically, the variance of the stochastic distribution of the digital output of the detector was measured, and $q_{0,0}$ in Eq. (9) was multiplied by a factor specific for the detector.[59]

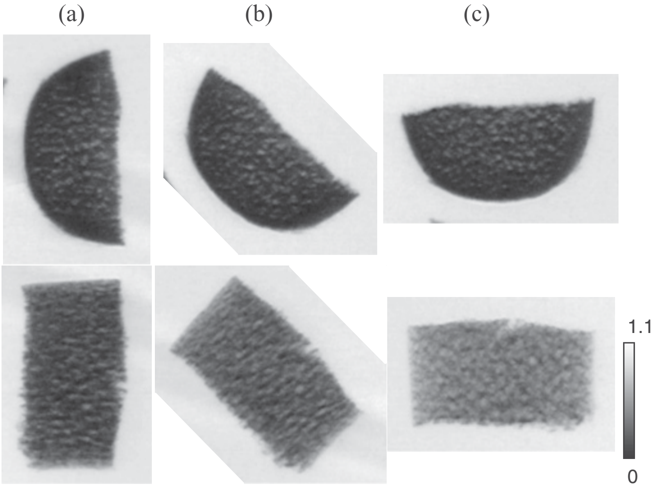

FIG. 3. Dependencies of visibility-contrast image on orientations of two samples in Fig. 2. (a) $\Phi = 0^\circ$, (b) $\Phi = 45^\circ$, and (c) $\Phi = 90^\circ$.

To investigate the origin of the anisotropy, we measured the pd dependence of the $-\ln(V/V_0)$ image [see Eq. (8)] by changing the distance between the two gratings. Figure 5(a) shows the experimental results for a pixel in the square of the image in Fig. 4(a) (crosses: $\Phi = 15^\circ$; filled circles: $\Phi = 60^\circ$; triangles: $\Phi = 105^\circ$). Solid, dashed, and dotted curves in the figure are the best-fit curves obtained using least-squares fittings with the model of Eq. (7). Good agreement with the experimental data indicates that the model is suitable even for describing a sample with anisotropic microstructures. From such a fitting, we obtained the correlation length ξ, the Hurst exponent H, and variance σ^2 of the phase fluctuations. Figures 5(b), 5(c), and 5(d) show the dependencies of ξ, H, and σ^2 on Φ for the pixel. The parameters ξ and H exhibited anisotropies and the former was more anisotropic than the latter, but σ^2 did not exhibit any anisotropy.

Similar to Fig. 4(b), sine functions plus constants fitted the dependencies of ξ, H, and σ^2 on Φ, and the angles $\Phi_{\max}$, where the parameters take the maximum values, as well as the amplitudes and the constants of the best-fit curves were obtained for each pixel in the square in Fig. 4(a). Figures 6(a), 6(b), and 6(c) are color representations of the anisotropies of ξ, H, and σ^2 in the square area (the color and brightness of the maps represent $\Phi_{\max}$ and the amplitudes of the best-fit sine curves). The ξ and H maps are green tinged and a bit red

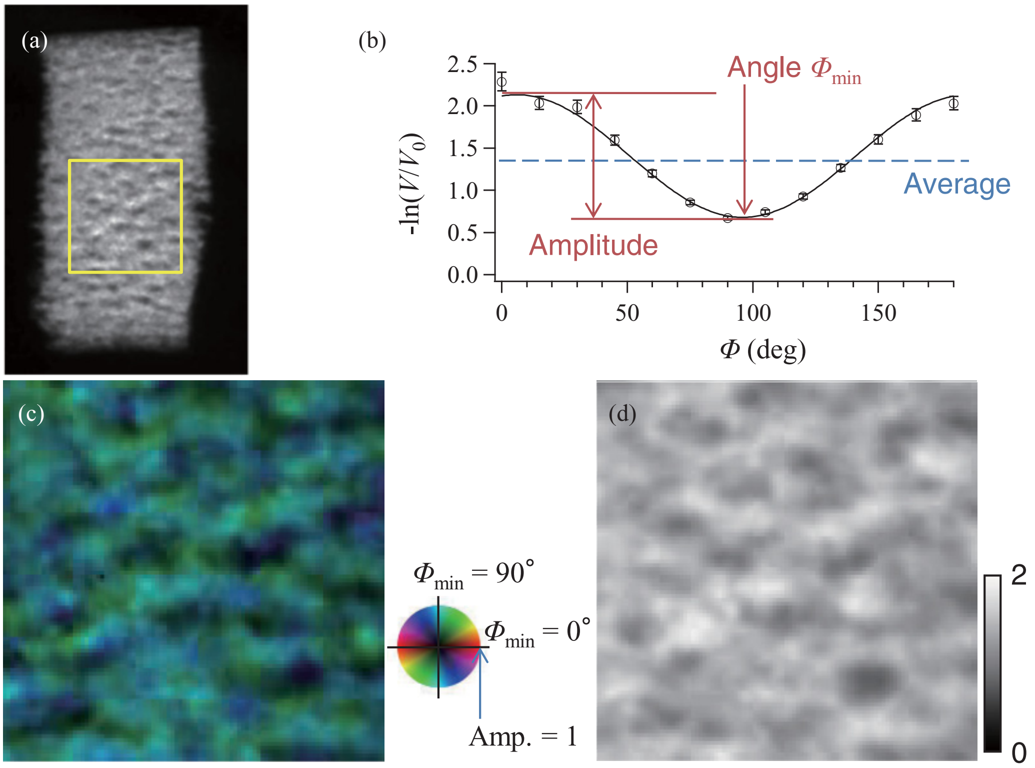

FIG. 4. (Color) (a) $-\ln(V/V_0)$ image at $\Phi = 0^\circ$ for lower sample in Fig. 3 ($p = 0.5$). (b) Dependence of $-\ln(V/V_0)$ on Φ for a pixel in square area in (a) ($p = 0.5$; open circles: experimental results; solid curve: best-fit sine function). (c) Color representation of anisotropy of $-\ln(V/V_0)$ in square area in (a) (color: Φ_{min}; brightness: amplitude of best-fit sine function). (d) Map of normalized visibility averaged over Φ in same area.

tinged, while the σ^2 map exhibits many different colors. In Figs. 6(d), 6(e), and 6(f), the amplitudes of the best-fit curves for 100 arbitrarily-chosen pixels in the square area are plotted against Φ_{max} for ξ, H, and σ^2 with their error bars. These

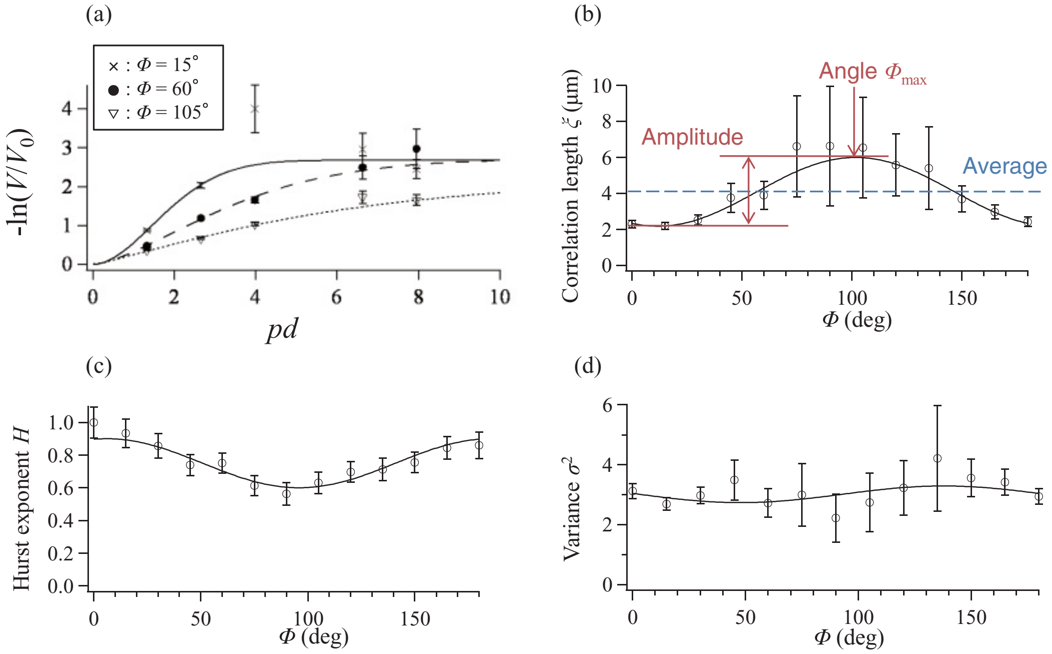

FIG. 5. (a) Experimental results of pd dependence of $-\ln(V/V_0)$ for a pixel in square area in Fig. 4(a) (crosses: $\Phi = 15^\circ$; filled circles: $\Phi = 60^\circ$; triangles: $\Phi = 105^\circ$). Solid, dashed, and dotted curves are best-fit curves obtained by least-squares fittings using model of Eq. (7). Dependencies of ξ, H, and σ^2 on Φ for the pixel are shown in (b), (c), and (d) (open circles) with best-fit sine functions (solid curves).

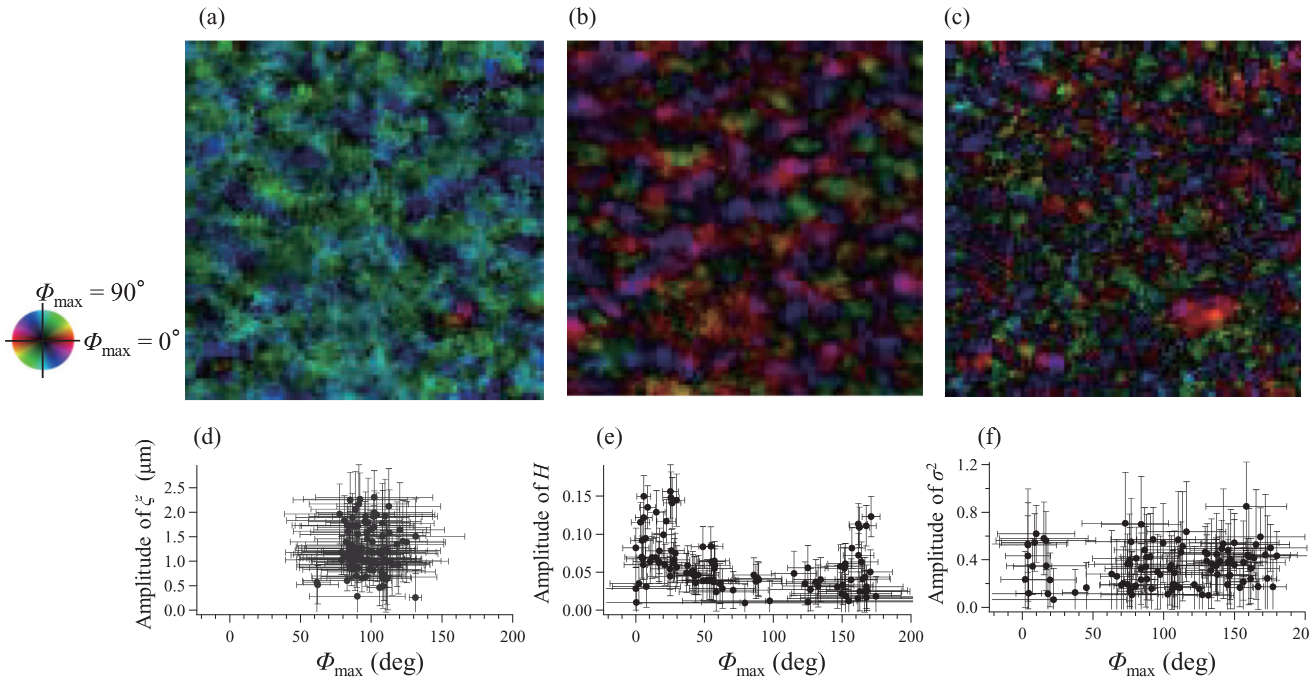

FIG. 6. (Color) Color representation of anisotropies of (a) ξ, (b) H, and (c) σ^2 in square area in Fig. 4(a) [brightness scales: 0 ~ 3 (a); 0 ~0.25 (b); 0 ~ 1.5 (c)]. Amplitudes of best-fit sine curves for 100 arbitrarily chosen pixels are plotted against $\Phi_{\max}$ for (d) ξ, (e) H, and (f) σ^2.

results show that ξ and H exhibit anisotropies, although the anisotropy of H was weaker than that of ξ, but σ^2 does not exhibit anisotropy, and that the anisotropy of the sample's visibility contrast mainly originated from that of ξ. This was also supported by the fact that the color distribution of the ξ map was similar to that of Fig. 4(c). In fact, the correlation coefficients of the color distributions of the ξ, H, and σ^2 maps with that of Fig. 4(c) were 0.53, 0.40, and 0.04, indicating that the anisotropy of normalized visibility mainly originated from that of ξ.

Figure 7(a) shows a map of the constant of the best-fit curve of σ^2 (corresponding to σ^2 averaged over Φ). As discussed in our previous paper,[51] σ^2 averaged over Φ should be proportional to the scattering power of the unresolvable microstructures in the forward direction, which is proportional to the sample thickness t if the sample is homogeneous, and the unresolvable microstructures are approximately regarded as particles, the positions and directions of which are independent of each other. Hence, Fig. 7(a) should correlate with the absorption image of the sample ($-\ln T$, where T is the transmittance of the sample) because $-\ln T$ is also proportional to t. Figure 7(b) shows a $-\ln T$ image of the sample. As we expected, there was a weak correlation between the images in Figs. 7(a) and 7(b) (their correlation coefficient for them was 0.35). The discrepancy between these images can be attributed to their contrast formation mechanisms; that is, the contrast of the image in Fig. 7(a) should be formed by the scattering power, which is proportional to not only t, but also the number density N of the unresolvable particles and the squared difference $(\Delta\rho)^2$ of the average number density of electrons in a particle from that of the matrix, while the contrast of the image in Fig. 7(b) is due to the absorption by the resolvable features.

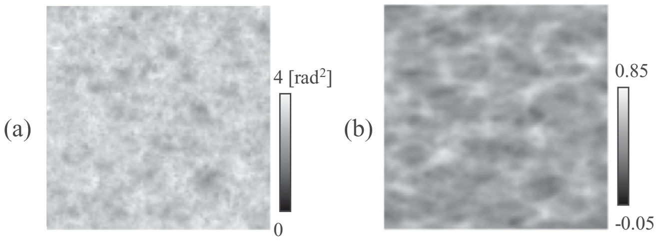

FIG. 7. (a) Map of σ^2 averaged over Φ and (b) absorption image ($-\ln T$ image, where T is transmittance of sample) in square area of image in Fig. 4(a).

IV. DISCUSSION

As we have shown using samples with isotropic microstructures,[51] the correlation length ξ of the autocorrelation function of the wavefront's spatial fluctuations due to unresolvable microstructures is related to the average size of the microstructure elements in the direction perpendicular to the grating lines. This should also be the case with a sample with anisotropic microstructures, as discussed in Sec. II. Our experimental results suggest that the average size of the microstructure elements along the cylinder axis is larger than that along the direction perpendicular to the cylinder axis. In fact, from the fittings as shown in Sec. III, we obtained a normalized autocorrelation function γ defined by Eq. (3) for each pixel in the square area in Fig. 4(a), and found that the shape of γ is typically elongated in the direction of the cylinder axis (see Fig. 8).

We also performed conventional absorption tomography and found that the resolvable structure of the material also

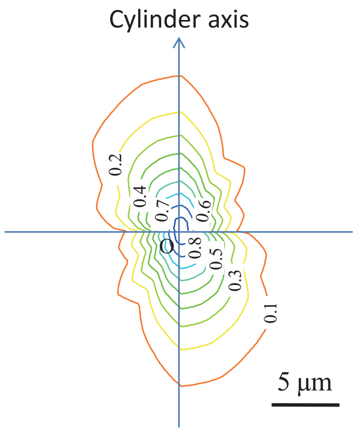

FIG. 8. (Color) Normalized autocorrelation function γ defined by Eq. (3) for a pixel.

has uniaxial anisotropy, the axis of which is parallel to the cylinder axis. Figure 9 shows example tomograms of the same material as those used for our experiment. From the section images of planes A and B, the sample seems to elongate in the direction parallel to the cylinder axis even when no force is applied. Although the structure resolved using absorption tomography cannot reduce visibility, the anisotropy of ξ is consistent with the results of the absorption tomograms if it is assumed that the unresolvable microstructure elements are elongated along the cylinder axis as well as the resolvable structure.

Finally, we discuss the possibility of visibility tomography. As we have discussed,[51] if a sample consists of homogeneous domains, each of which is larger than the size that can be resolved with the detector and has no structural correlation with the others, normalized visibility can be expressed by

$$\frac{V}{V_0} \approx \exp\left[-\sum_j \sigma_j^2\{1-\gamma_j\}\right], \tag{10}$$

where j represents the contribution from the jth domain on the path to a pixel along the z axis [see Eq. (2)]. Because σ_j^2 should be proportional to the thickness of the jth domain, Eq. (10) has a similar form to the Beer-Lambert law.[60] As a result, $-\ln(V/V_0)$ can be given by

$$-\ln\left(\frac{V}{V_0}\right) \approx \int \frac{\partial(\sigma(z)^2)}{\partial z}\{1-\gamma(z)\}dz, \tag{11}$$

where σ and γ are expressed as a function of z. Thus, we can also carry out visibility tomography and determine the three-dimensional distribution of $(1-\gamma)\partial(\sigma^2)/\partial z$ for a sample with isotropic microstructures.

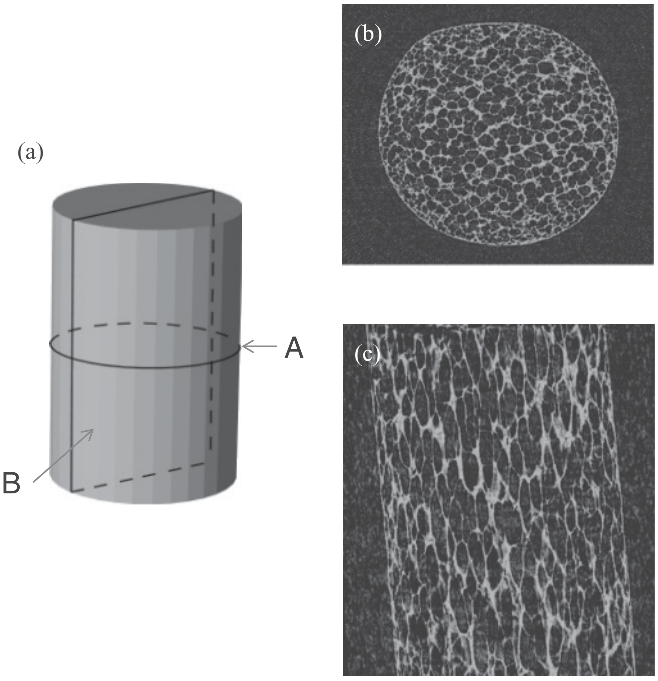

FIG. 9. Absorption tomograms of CR sponge used in our experiment. (a) Schematic view of sample; (b) and (c) are section images along planes A and B.

It should be noted that for a sample with anisotropic microstructures, the rotation axis for visibility tomography has to be perpendicular to the grating lines because, for it to be correctly performed, $(1-\gamma)\partial(\sigma^2)/\partial z$ in Eq. (11) has to be unchanged by the rotation (otherwise the projection ϕ_f of the microstructures at a voxel can change during the rotation). For the same reason, laminography, where the rotation axis is inclined,[61,62] cannot be performed easily.

For a sample with isotropic microstructures, tomographies for $\partial(\sigma^2)/\partial z$, ξ, and H can be easily achieved because they are not functions of the sample orientation. To perform $\partial(\sigma^2)/\partial z, \xi$, and H tomographies for a sample with anisotropic microstructures, we also have to rotate the rotation axis of the sample around the optical axis. Finally, we can obtain a tomogram, each voxel of which accompanies a characteristic three-dimensional shape of the microstructure inside the voxel.

V. CONCLUSION

We proposed a method for mapping distributions of parameters characterizing unresolvable anisotropic microstructures in a sample from visibility-contrast images obtained using x-ray Talbot interferometry. In Sec. II we briefly reviewed the theoretical background, where general formulas for the visibility contrast based on the spatial fluctuations of a wavefront were provided [Eqs. (1) and (8)]. In Sec. III we applied our method to a CR sponge, which exhibited uniaxial anisotropy of visibility contrast (Fig. 3). Dependence of visibility contrast on the Talbot order was measured for each orientation of the sample, and the result for each pixel was fitted using the simple model of Eq. (7) [for example, Fig. 5(a)]. From such a least-squares fitting, we obtained optimal values of three parameters, the correlation length, the Hurst exponent, and variance, which characterize the phase fluctuations due to the unresolvable microstructures in the sample, and we obtained their dependencies on the sample orientation [for example, Figs. 5(b), 5(c), and 5(d)]. By fitting sine functions to these dependencies, we obtained maps that represent anisotropies of the three parameters [Figs. 6(a), 6(b), and 6(c)]. We found that the correlation length [Figs. 6(a) and 6(d)] and the Hurst exponent [Figs. 6(b) and 6(e)] exhibited anisotropies and the former was more anisotropic than the latter, but the variance [Figs. 6(c) and 6(f)] did not exhibit any anisotropies. These results indicated that the anisotropy of visibility contrast mainly originated from the anisotropy of the correlation length, that is, the anisotropy of the microstructure elements' average size. This was also supported by the fact that the color representation of the anisotropy of the correlation length was similar to that obtained for the anisotropy of visibility contrast [Figs. 6(a) and 4(c)]. In Sec. IV we showed an example of normalized autocorrelation function γ obtained from the experiment (Fig. 8), and discussed the origin of the anisotropy of the microstructure elements' average size by comparing it with a result from conventional absorption tomography. Future prospects, for example, visibility tomography for a sample with anisotropic microstructures, were also raised. Our method should become a useful tool for investigating, for example, fiber (tubular) and particle (porous) structures in material, biological, and medical samples and have broad applications in various fields.

ACKNOWLEDGMENTS

We would like to show our appreciation to Professor Tadashi Hattori and Dr. Daiji Noda for their fabrication of the gratings and Dr. Kazuyuki Hyodo for his assistance in the experiments. The experiments were performed at Photon Factory (2009G031). This study was financially supported by the Japan Science and Technology Agency (JST) and the Konica Minolta Science and Technology Foundation.

---

[*] yashiro@mml.k.u-tokyo.ac.jp

[1] R. Fitzgerald, Phys. Today **53**, 23 (2000).

[2] A. Momose, Jpn. J. Appl. Phys. **44**, 6355 (2005).

[3] K. A. Nugent, Adv. Phys. **59**, 1 (2010).

[4] A. Momose, S. Kawamoto, I. Koyama, Y. Hamaishi, K. Takai, and Y. Suzuki, Jpn. J. Appl. Phys. **42**, L866 (2003).

[5] T. Weitkamp, A. Diaz, B. Nöhammer, F. Pfeiffer, T. Rohbeck, P. Cloetens, M. Stampanoni, and C. David, Proc. SPIE **5535**, 137 (2004).

[6] A. Momose, S. Kawamoto, I. Koyama, and Y. Suzuki, Proc. SPIE **5535**, 352 (2004).

[7] T. Weitkamp, B. Nöhammer, A. Diaz, C. David, and E. Ziegler, Appl. Phys. Lett. **86**, 054101 (2005).

[8] T. Weitkamp, A. Diaz, C. David, F. Pfeiffer, M. Stampanoni, P. Cloetens, and E. Ziegler, Opt. Express **13**, 6296 (2005).

[9] F. Pfeiffer, T. Weitkamp, O. Bunk, and C. David, Nat. Phys. **2**, 258 (2006).

[10] M. Engelhardt, J. Baumann, M. Schuster, C. Kottler, F. Pfeiffer, O. Bunk, and C. David, Appl. Phys. Lett. **90**, 224101 (2007).

[11] A. Olivo and R. Speller, Appl. Phys. Lett. **91**, 074106 (2007).

[12] F. Pfeiffer, M. Bech, O. Bunk, P. Kraft, E. F. Eikenberry, C. H. Brönnimann, C. Grünzweig, and C. David, Nat. Mater **7**, 134 (2008).

[13] Y. I. Nesterets and S. W. Wilkins, Opt. Express **16**, 5849 (2008).

[14] Y. Takeda, W. Yashiro, T. Hattori, A. Takeuchi, Y. Suzuki, and A. Momose, Appl. Phys. Exp. **1**, 117002 (2008).

[15] W. Yashiro, Y. Takeda, and A. Momose, J. Opt. Soc. Am. A **25**, 2025 (2008).

[16] A. Momose, W. Yashiro, H. Maikusa, and Y. Takeda, Opt. Express **17**, 12540 (2009).

[17] A. Momose, W. Yashiro, and Y. Takeda, in *Biomedical Mathematics: Promising Directions in Imaging, Therapy Planning and Inverse Problems*, edited by Y. Censor and M. Jiang (Medical Physics Publishing, Madison, WI, 2009), Ch. 14.

[18] C. P. Richter, S. Shintani-Smith, A. Fishman, C. David, I. K. Robinson, and C. Rau, Micro. Res. Tech. **72**, 902 (2009).

[19] T. Donath, M. Chabior, F. Pfeiffer, O. Bunk, E. Reznikova, J. Mohr, E. Hempel, S. Popescu, M. Hoheisel, M. Schuster, J. Baumann, and C. David, J. Appl. Phys. **106**, 054703 (2009).

[20] Z. F. Huang, K. J. Kang, L. Zhang, Z. Q. Chen, F. Ding, Z. T. Wang, and Q. G. Fang, Phys. Rev. A **79**, 013815 (2009).

[21] A. Olivo, S. E. Bohndiek, J. A. Griffiths, A. Konstantinidis, and R. D. Speller, Appl. Phys. Lett. **94**, 044108 (2009).

[22] W. Yashiro, Y. Takeda, A. Takeuchi, Y. Suzuki, and A. Momose, Phys. Rev. Lett. **103**, 180801 (2009).

[23] Z. F. Huang, Z. Q. Chen, L. Zhang, K. Kang, F. Ding, Z. T. Wang, and H. Z. Ma, Opt. Express **18**, 10222 (2010).

[24] P. Zhu, K. Zhang, Z. Wang, Y. Liu, X. Liu, Z. Wu, S. McDonald, F. Marone, and M. Stampanoni, Proc. Natl. Acad. Sci. **107**, 13576 (2010).

[25] D. Stutman, M. Finkenthal, and N. Moldovan, Appl. Opt. **49**, 4677 (2010).

[26] W. Yashiro, S. Harasse, A. Takeuchi, Y. Suzuki, and A. Momose, Phys. Rev. A **82**, 043822 (2010).

[27] C. Kottler, V. Revol, R. Kaufmann, and C. Urban, J. Appl. Phys. **108**, 114906 (2010).

[28] F. Krejci, J. Jakubek, and M. Kroupa, J. Instrum. **6**, C01073 (2011).

[29] G. H. Chen, J. Zambelli, K. Li, N. Bevins, and Z. H. Qi, Med. Phys. **38**, 584 (2011).

[30] K. S. Morgan, D. M. Paganin, and K. K. W. Siu, Opt. Lett. **36**, 55 (2011).

[31] H. Itoh, K. Nagai, G. Sato, K. Yamaguchi, T. Nakamura, T. Kondoh, C. Ouchi, T. Teshima, Y. Setomoto, and T. Den, Opt. Express **19**, 3339 (2011).

[32] I. Zanette, M. Bech, F. Pfeiffer, and T. Weitkamp, Appl. Phys. Lett. **98**, 094101 (2011).

[33] A. Momose, W. Yashiro, S. Harasse, and H. Kuwabara, Opt. Express **19**, 8423 (2011).

[34] A. Momose, H. Kuwabara, and W. Yashiro, Appl. Phys. Exp. **4**, 066603 (2011).

[35] H. Kuwabara, W. Yashiro, H. Harasse, H. Mizutani, and A. Momose, Appl. Phys. Exp. **4**, 062502 (2011).

[36] J. H. Bruning, D. R. Herriott, J. E. Gallagher, D. P. Rosenfeld, A. D. White, and D. J. Brangaccio, Appl. Opt. **13**, 2693 (1974).

[37] H. Schreiber and J. H. Bruning, in *Optical Shop Testing*, edited by D. Malacara (Wiley Interscience, New York, 2007), Ch. 14.

[38] E. Hack and J. Burke, Rev. Sci. Instrum. **82**, 061101 (2011).

[39] C. Grünzweig *et al.*, Phys. Rev. Lett. **101**, 025504 (2008).

[40] M. Strobl, C. Grünzweig, A. Hilger, I. Manke, N. Kardjilov, C. David, and F. Pfeiffer, Phys. Rev. Lett. **101**, 123902 (2008).

[41] C. Grünzweig, C. David, O. Bunk, M. Dierolf, G. Frei, G. Kuhne, R. Schafer, S. Pofahl, H. M. R. Ronnow, and F. Pfeiffer, Appl. Phys. Lett. **93**, 112504 (2009).

[42] F. Pfeiffer, M. Bech, O. Bunk, T. Donath, B. Henrich, P. Kraft, and C. David, J. Appl. Phys. **105**, 102006 (2009).

[43] S. A. MacDonald, F. Marone, C. Hintermüller, G. Mikuljan, C. David, F. Pfeiffer, and M. Stampanoni, J. Synchrotron Radiat. **16**, 562 (2009).

[44] H. Wen, E. E. Bennett, M. M. Hegedus, and S. Rapacchi, Radiology **251**, 910 (2009).

[45] Z. T. Wang, K. J. Kang, Z. F. Huang, and Z. Q. Chen, Appl. Phys. Lett. **95**, 094105 (2009).

[46] T. H. Jensen, M. Bech, O. Bunk, T. Donath, C. David, R. Feidenhans'l, and F. Pfeiffer, Phys. Med. Biol. **55**, 3317 (2010).

[47] M. Bech, O. Bunk, T. Donath, R. Feidenhans'l, C. David, and F. Pfeiffer, Phys. Med. Biol. **55**, 5529 (2010).

[48] G. H. Chen, N. Bevins, J. Zambelli, and Z. H. Qi, Opt. Express **18**, 12960 (2010).

[49] I. Manke, N. Kardjilov, R. Schäfer, A. Hilger, M. Strobl, M. Dawson, C. Grünzweig, G. Behr, M. Hentschel, C. David, A. Kupsch, A. Lange, and J. Banhart, Nat. Commun. **1**, 125 (2010).

[50] T. H. Jensen, M. Bech, I. Zanette, T. Weitkamp, C. David, H. Deyhle, S. Rutishauser, E. Reznikova, J. Mohr, R. Feidenhans'l, and F. Pfeiffer, Phys. Rev. B **82**, 214103 (2010).

[51] W. Yashiro, Y. Terui, K. Kawabata, and A. Momose, Opt. Express **18**, 16890 (2010).

[52] Y. I. Nesterets, Opt. Commun. **281**, 533 (2008).

[53] I. A. Vartanyants and I. K. Robinson, Opt. Commun. **222**, 29 (2003).

[54] K. Patorski, *Progress in Optics* XXVII, edited by E. Wolf (Elsevier Science, New York, 1989).

[55] S. K. Sinha, E. B. Sirota, S. Garoff, and H. B. Stanley, Phys. Rev. B **38**, 2297 (1988).

[56] For a sample with strongly anisotropic microstructures, γ should be more generally given by a function of X/ξ that satisfies $\gamma = 1$ and 0 for $X = 0$ and ∞.

[57] W. Yashiro, Y. Terui, K. Kawabata, and A. Momose, AIP Conf. Proc. (to be published).

[58] C. J. Morgan, Opt. Lett. **7**, 368 (1982).

[59] V. Revol, C. Kottler, R. Kaufmann, U. Straumann, and C. Urban, Rev. Sci. Instrum. **81**, 073709 (2010).

[60] *Handbook of Optics*, 2nd ed., edited by M. Bass, J. M. Enoch, E. W. Van Stryland, and W. L. Wolfe (McGraw-Hill, New York, 1994), Vol. 1.

[61] L. Helfen, T. Baumbach, P. Mikulik, D. Kiel, P. Pernot, P. Cloetens, and J. Baruchel, Appl. Phys. Lett. **86**, 071915 (2005).

[62] L. Helfen, T. Baumbach, P. Cloetens, and J. Baruchel, Appl. Phys. Lett. **94**, 104103 (2009).